Soft Matter

PAPER

View Article Online
View Journal | View Issue

Cite this: *Soft Matter*, 2016, **12**, 7056

Investigating the role of a poorly soluble surfactant in a thermally driven 2D microfoam†

Vincent Miralles,[a] Emmanuelle Rio,[b] Isabelle Cantat[c] and Marie-Caroline Jullien*[a]

Received 21st March 2016,
Accepted 19th July 2016

DOI: 10.1039/c6sm00686h

www.rsc.org/softmatter

Foam drainage dynamics is known to be strongly affected by the nature of the surfactants stabilising the liquid/gas interface. In the present work, we consider a 2D microfoam stabilized by both soluble (sodium dodecylsulfate) and poorly soluble (dodecanol) surfactants. The drainage dynamics is driven by a thermocapillary Marangoni stress at the liquid/gas interface [V. Miralles *et al.*, *Phys. Rev. Lett.*, 2014, **112**, 238302] and the presence of dodecanol at the interface induces interface stress acting against the applied thermocapillary stress, which slows down the drainage dynamics. We define a damping parameter that we measure as a function of the geometrical characteristics of the foam. We compare it with predictions based on the interface rheological properties of the solution.

1 Introduction

Foams are ubiquitous in everyday life, and for fields as varied as enhanced oil recovery[1,2] or solid foams,[3,4] a major stake in terms of controlling foam properties is to understand the dynamics of drainage, a key destabilisation process.[5–8] Our insight into foam drainage has been steadily refined since the pioneering work of Leonard and Lemlich.[9] Two important models rationalized two distinct regimes, where dissipation is dominant in either the Plateau borders or the nodes, respectively: the Trinity College model considers a rigid interface, with an infinite surface shear viscosity and a Poiseuille flow in the Plateau borders (dissipation in the borders),[10] while the Harvard model is based on a zero surface shear viscosity and a plug flow in the Plateau borders, *i.e.* the interface is fluid (dissipation in the nodes)[6,11] – both models perform well in their respective forced-drainage set of experiments.[12] Experimental transitions between these two regimes were observed depending on the liquid fraction[13] or the Boussinesq number $B_q = \varepsilon/(\eta R_{\mathrm{Pb}})$[14] that compares surface and bulk viscous dissipations through the interface shear viscosity ε, the bulk dynamic viscosity η and the radius of curvature of the Plateau borders R_{Pb}. A main take-away from these models is that the physical chemistry of the components forming the foam (*i.e.* the surfactants, liquid and gas) significantly impacts the predictions of the global drainage model by changing the boundary condition at the gas/liquid interface:[15]

$$(\bar{\mathbf{P}}_{\mathrm{gas}} - \bar{\mathbf{P}}_{\mathrm{sol}})\mathbf{n} = \nabla_s \cdot \bar{\mathbf{P}}^{\mathrm{s}} \quad (1)$$

where $\mathbf{n}$ is the normal to the interface oriented towards the liquid phase, $\bar{\mathbf{P}}_{\mathrm{gas}} = -p_0\bar{\mathbf{I}}$ and $\bar{\mathbf{P}}_{\mathrm{sol}} = -p\bar{\mathbf{I}} + \bar{\tau}$ are the stress tensors, respectively, in the gas and liquid phases and $\bar{\mathbf{P}}^{\mathrm{s}} = \bar{\mathbf{I}}_{\mathbf{s}}\gamma + \bar{\tau}^{\mathrm{s}}$ is the surface-excess stress, with γ being the surface tension and $\bar{\tau}^{\mathrm{s}}$ being the viscous contribution involving the surface shear viscosity ε and the surface dilational viscosity κ.

Importantly, the Marangoni stress $\nabla_s \cdot \bar{\mathbf{I}}_{\mathbf{s}}\gamma$, due to surface tension variations, can contain two contributions: (i) the thermocapillary stress $\partial_T\gamma\partial_x T$, and (ii) the Gibbs Marangoni stress $\partial_\Gamma\gamma\partial_x\Gamma$, which comes from a non-homogeneous surface concentration of surfactant, Γ. The importance of the Gibbs contribution was explored by Durand and Langevin,[16] who worked within Leonard and Lemlich's framework but included surface tension variations due to a gradient in the surface concentration of surfactants. Remarkably, their model was able to account for both the Harvard and Trinity regimes, and for insoluble surfactants with a dissipation occurring only in the Plateau borders. This work was then refined to include a recirculating flow at the junction of the Plateau borders and the films, due to the Marangoni stress;[17] in this picture, the films act as a surfactant reservoir.

The present study attempts to shed more light on this issue by taking advantage of a microfluidic experimental setup in which the geometry is very simple and the parameters are well controlled. More precisely, we study the drainage dynamics of a microfoam constrained in a 2D microfluidic Hele-Shaw cell. The geometry of the 2D foam is then very simple: a single layer of monodisperse bubbles of controlled radius R, where the cross-section of the Plateau borders is set by the height of the

---

[a] MMN, Laboratoire Gulliver, CNRS, ESPCI Paris, PSL Research University, 10 rue Vauquelin, 75005 Paris, France. E-mail: marie-caroline.jullien@espci.fr; Tel: +33 1 40 79 41 61

[b] Laboratoire de Physique des Solides, UMR CNRS & Université Paris-Sud 8502, 91405 Orsay Cedex, France

[c] IPR, UMR CNRS 6251, Université de Rennes 1, 35000 Rennes, France

† Electronic supplementary information (ESI) available. See DOI: 10.1039/c6sm00686h

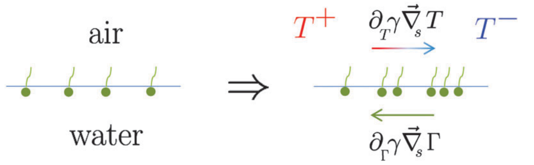

Fig. 1 Illustration of the Marangoni stress at the air–water interface. DOH molecules are represented in green. Left: The interface is at rest and the surfactants are homogeneously distributed. Right: A temperature gradient induces a thermocapillary stress ($\partial_T\gamma\vec{\nabla}_s T$, where $\vec{\nabla}_s$ is the surface gradient) that affects the surfactant distribution, causing in turn a solutocapillary stress ($\partial_\Gamma\gamma\vec{\nabla}_s\Gamma$) in the opposite direction.

chamber $e \ll R$.[18,19] The cell is placed horizontally on a series of heating resistors, which allows us to impose a well-defined local temperature gradient and use the thermocapillary component of the Marangoni stress as a driving force. We previously used a similar setup to characterize the drainage dynamics of a foam stabilized by the highly soluble surfactant sodium dodecylsulfate (SDS), and were able to show that surface rheology played no role in that situation.[20] Here, we add a poorly soluble surfactant to the solution, dodecanol (DOH), that adsorbs on the interface. During drainage, the air/liquid interfaces move towards the cooler part of the bubble in response to the thermocapillary driving stress $\partial_T\gamma\partial_x T$, advecting the DOH. The dodecanol then accumulates at the cooler end of the bubble, inducing in turn a solutocapillary stress opposing drainage: $\partial_\Gamma\gamma\partial_x\Gamma$, where Γ is the dodecanol surface excess, see Fig. 1. In addition to this Gibbs elasticity effect, the surface shear and dilational viscosities are expected to increase with the DOH concentration at the interface, which would also contribute to slowing down the drainage process. We indeed find that the characteristic time t_d of the drainage process is increased by a maximal factor of 20% due to the addition of DOH to the solution. To assess the influence of these different contributions, we measure the variation of t_d with the temperature gradient (driving term), the DOH concentration, and the geometrical parameters R and e.

We then cover several possible models, looking for a dominant contribution. For each of the mechanisms listed above, we derive the relative scaling law for a characteristic damping parameter r with respect to the geometrical parameters of the system, and compare it with our experimental data. While looking at the Gibbs elasticity in particular, we also consider different ways to formalize the diffusion of surfactants from one bubble to the next. However, none of these models turn out to be sufficient to capture the full picture, which leads us to conclude that even in such a minimal system, the drainage dynamics probably results from a complex interplay between several contributions.

2 Materials and methods

The experimental setup is a microfluidic Hele-Shaw cell placed horizontally on a series of heating resistors, see the inset in Fig. 2. The chamber is made of polydimethylsiloxane (PDMS) and fabricated using standard soft lithography techniques.[21] Its dimensions are $L \times w = 2000 \times 1500\ \mu\text{m}^2$ in the plane, with a thickness $e \in \{19.3;54.2\}\ \mu\text{m}$. The optimized resistors placed below the cell generate a linear temperature profile along x, while the temperature is homogeneous along y, which induces a constant thermocapillary stress throughout the foam: $d_x\gamma = \partial_x T\partial_T\gamma$.[22] The temperature range is [25–32] °C, which corresponds to a constant thermocapillary stress equal to 0.735 Pa for all experiments. This thermocapillary stress is the only driving force inducing drainage, since the cell is placed horizontally in the (x,y) plane, and gravity (along z) plays no role. We characterize the drainage dynamics by following the time evolution of the liquid fraction ϕ *via* image processing.[20]

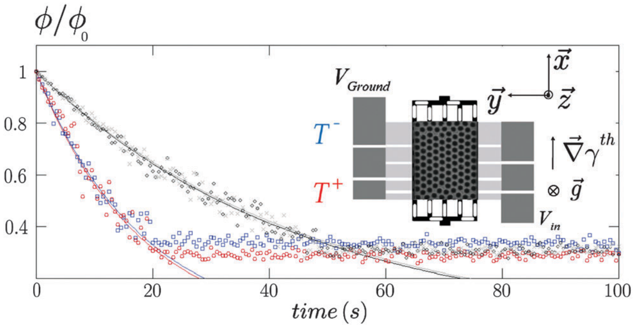

Fig. 2 Typical time evolution of the liquid volume fraction ϕ normalised by the liquid fraction at initial time $\phi_0 \sim 14\%$. The thermocapillary stress is set to a constant value equal to 0.735 Pa for all the experiments. Open circles and open squares, respectively, correspond to [DOH] $\in \{1.6 \times 10^{-6}; 5.6 \times 10^{-6}\}$ mol L^{-1} and e = 54.2 μm. Open diamonds and crosses, respectively, correspond to [DOH] $\in \{1.6 \times 10^{-6}; 5.6 \times 10^{-6}\}$ mol L^{-1} and e = 19.3 μm. Solid lines show the best exponential fit for each dataset. Error bars are within 10% for all the experimental curves, and are not represented to help legibility. Inset: Sketch of the experimental setup. The Hele-Shaw cell is sealed above the heating resistors.[20]

The foaming solution consists of SDS (Sigma-Aldrich, 16 mM – 2 cmc – at 25 °C) with DOH (Fluka, at concentrations that will be given throughout the paper) mixed with glycerol (5.68 wt%, Aldrich) in deionized water (Millipore). In the following, the DOH bulk concentration will be noted either [DOH] in the graphs, or simply c in the equations. The bulk viscosity of the solution is η = 1.2×10^{-3} Pa s at 25 °C and 0.88×10^{-3} Pa s at 32 °C[23] and does not depend on the DOH concentration: this means a relative variation of about 10% in our temperature range, which lies within the error bars of our results. Moreover, a noticeable influence of the variation of η with the temperature would lead to nonlinear variations of the flows with the temperature, which was carefully ruled out in previous work using a similar setup.[20] We thus assume a constant value of $\eta = 1.2 \times 10^{-3}$ Pa s in the following. As regards the shear viscosity of the solution, it is very low and difficult to measure; our discussion only considers the order of magnitude of this viscosity. The values reported in the literature are $\eta_s = 6 \times 10^{-8}$ kg s^{-1} for SDS at 2 cmc and $\eta_s = 2 \times 10^{-6}$ kg s^{-1} when 0.3 g L^{-1} of DOH is added, with relative error bars of ~25%.[24] The variations with temperature in our operating range are unknown, but probably well within these error bars. Finally, the surface tension of the solution has been measured as a function of temperature and DOH concentration and is given in the ESI.†

3 Experimental results

The drainage process is monitored by following the normalized liquid fraction ϕ/ϕ_0 over time, where ϕ_0 is the initial liquid fraction. The specific case of a solution containing SDS as the only surfactant has been extensively investigated in a previous work,[20] and is used as a reference point in what follows. The foaming solution is driven by the thermocapillary stress towards the cooler end of the cell, where it is free to exit. This corresponds to an exponential decrease in ϕ down to a saturation value at $t = t_s$. Fig. 2 shows the time evolution of ϕ/ϕ_0 for high and low DOH concentrations, at two different values of the cell thickness e, as well as the corresponding exponential fits $\phi(t) = \phi_0 e^{-t/t_d}$ over the time range $[0\text{–}t_s]$. As expected, introducing DOH in the solution slows down the drainage process, and t_d varies with the DOH concentration for both values of e (we carefully checked that the characteristic drainage time t_d is insensitive to the choice of the cut-off time t_s, which can vary within a few seconds without notably affecting t_d).

To quantify the influence of dodecanol in the solution, we introduce a damping factor r, directly related to the experimental t_d, measuring the departure from the reference case. First, the mass conservation equation in the cell gives:

$$\frac{\mathrm{d}\ln\phi}{\mathrm{d}t} = -\frac{\bar{v}_x}{L} \tag{2}$$

where $\bar{v}_x$ is the projection along x of the average velocity in the liquid phase near the cell end and L is the cell's length.[20] In the reference case, we proposed to neglect all the rheological properties of the interface, and could write:

$$\bar{v}_x^0 = \frac{\alpha e}{\eta}\partial_T\gamma\partial_x T \tag{3}$$

with a numerical parameter α observed experimentally to be constant within 3% and equal to $\alpha_0 = 3.7 \times 10^{-3}$ whatever the values of the bubble radius R (defined in Fig. 6) and the cell thickness e.[20] As will be discussed in more detail in Section 4, the corrections related to the different rheological properties of the interface all depend on these two geometrical parameters, and the independence of α with respect to R and e confirmed our initial assumption that the rheological properties of the SDS solution are negligible in our system.

The damping factor r can now be defined by setting:

$$\bar{v}_x = \bar{v}_x^0(1 - r). \tag{4}$$

Using $\phi = \phi_0\exp(-t/t_d)$ and eqn (2), we get the direct relation between r and the experimentally measured t_d:

$$t_d = \frac{\eta L}{\alpha_0 e(1-r)\partial_T\gamma\partial_x T}. \tag{5}$$

We can now look at the influence of the temperature gradient, the dodecanol concentration, the bubble size R and the cell thickness e on the damping parameter r, see Fig. 3 and 4. First, we find that for a given DOH concentration and geometry, the value of r does not depend on the applied temperature gradient (inset in Fig. 3), *i.e.* the system responds linearly to the driving stress. This confirms that the temperature dependence of all the physical parameters is negligible. Consequently and for the sake of simplicity, the thermocapillary stress is set to a constant value equal to $\partial_T\gamma\partial_x T = 0.735$ Pa in all the following experiments, corresponding to $\partial_T\gamma = -2.1 \times 10^{-4}$ N m^{-1} K^{-1} and $\partial_x T = -3.5$ K mm^{-1}.

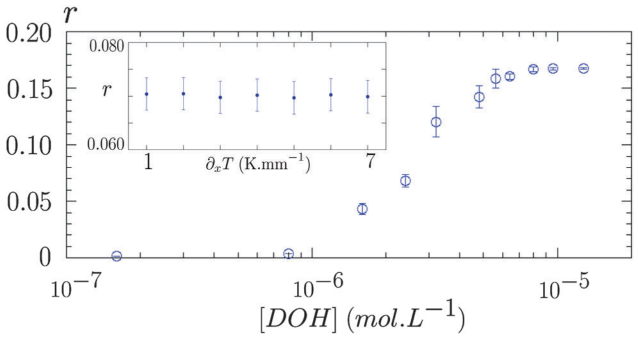

Fig. 3 Damping factor r as a function of the DOH bulk concentration, for $e = 54.2$ μm and $R = 86.0 \pm 2.9$ μm ($e/R = 0.63$). Inset: Evolution of r as a function of the applied temperature gradient, with [DOH] = 3.2×10^{-6} mol L^{-1} and $e/R = 0.53 \pm 0.02$.

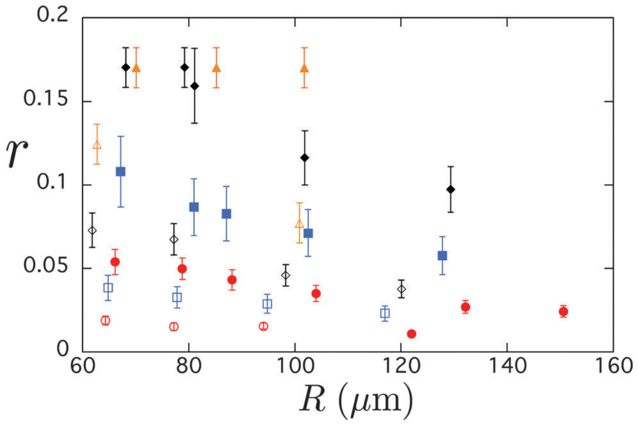

Fig. 4 Evolution of r as a function of the bubble radius R for different DOH concentrations and different cell thicknesses e: 1.6×10^{-6} mol L^{-1} (circles), 3.2×10^{-6} mol L^{-1} (squares), 5.6×10^{-6} mol L^{-1} (diamonds) and 9.6×10^{-6} mol L^{-1} (triangles). For each dataset, the hollow (resp. solid) symbols correspond to $e = 19.3$ μm (resp. $e = 54.2$ μm).

The evolution of r with the DOH concentration is shown in Fig. 3, for typical values of the geometrical parameters $e = 54.2$ μm and $R = 86.0 \pm 2.9$ μm ($e/R = 0.63$). We find that $r = 0$ below a DOH concentration of $c \sim 10^{-6}$ mol L^{-1}: at such low concentrations, there are not enough DOH molecules adsorbed at the interface to significantly affect the interface stress tensor. At higher concentrations however, the increase of r is a signature of the appearance of an additional interface stress, until a plateau is reached above $c = 10^{-5}$ mol L^{-1} where $r = 0.17$. Importantly, the presence of dodecanol never rigidifies the interface enough to induce an interfacial stress able to fully counteract the thermocapillary stress. In other words, we never reach the rigid interface limit proposed in the Trinity College model.

Lastly, Fig. 4 shows the variation of r with the two relevant geometrical quantities: the typical length of a meniscus R

and its width e. As discussed previously, the characteristic drainage time does not depend on e or R in the absence of DOH (see eqn (3)): $r = 0$ in the reference case. Conversely, for DOH concentrations in the range $[10^{-6}–10^{-5}]$ mol L^{-1}, r increases with e and decreases with R, until saturation is reached at $r = 0.17$. Such a geometry-dependent delay is the signature of interfacial rheology effects due to the presence of DOH.

4 Model

To gain better insight into the relative contributions of the surface shear viscosity ε, the dilational viscosity κ, and the solutocapillary effect, we look for scaling laws for r (with the parameters e, R and ∇T) corresponding to each of the mechanisms at play. To do so, we write down the full boundary conditions at the interface.

We take the meniscus in contact with the plate, separating two bubbles as an elementary piece of foam, see Fig. 5. In our range of liquid fractions, there is no film between adjacent bubbles, and the transverse radius of curvature of the meniscus is $e/2$. Since the foam is squeezed between two plates with $e \ll R$, the second curvature is negligible, and each air/liquid interface is a fraction of a cylinder of radius $e/2$. The orientation of the local normal $\vec{n}$ and tangent $\vec{t}$ on the interface is given in Fig. 5. For the sake of simplicity, the equations are written for a meniscus parallel to the x direction. Inside the bubbles, the pressure is constant and equal to p_0, and the viscous stress is negligible; gravity and inertia can also be safely neglected. In our geometry, the width e of the meniscus cannot vary and some degrees of freedom are thus blocked: in particular, an isotropic extension, which would induce forces involving κ only, cannot occur. Here, the interface may only be (i) sheared in the (t,x) plane, and (ii) elongated along x. Case (i) is a simple shear and involves only ε. Case (ii) is, from geometrical arguments, a mix of simple shear and isotropic extension. The combination of viscosities corresponding to this uniaxial stretching is $\varepsilon + \kappa$. This can be mathematically derived by writing the boundary conditions at the gas/liquid interface (domain $\partial\Omega_1$ in Fig. 5), which are:[25]

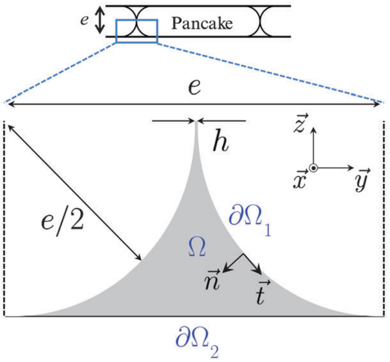

Fig. 5 Zoom in on the cross-sectional view of a pseudo-Plateau border, and definition of domains (the liquid phase is represented in grey).

Normal stress component:

$$p - p_0 - 2\eta\frac{\partial v_n}{\partial n} = -\frac{2}{e}\left[\gamma + \kappa\left(\frac{\partial v_t}{\partial t}+\frac{\partial v_x}{\partial x}\right) + \varepsilon\left(\frac{\partial v_t}{\partial t}-\frac{\partial v_x}{\partial x}\right)\right], \tag{6}$$

Stress component along $\vec{t}$:

$$\eta\left(\frac{\partial v_t}{\partial n}-\frac{2v_t}{e}\right) = -\left[\frac{\partial\gamma}{\partial t}+\kappa\frac{\partial}{\partial t}\left(\frac{\partial v_t}{\partial t}+\frac{\partial v_x}{\partial x}\right)+\varepsilon\left(\frac{\partial^2 v_t}{\partial t^2}+\frac{\partial^2 v_t}{\partial x^2}\right)\right] \tag{7}$$

Stress component along $\vec{x}$:

$$\eta\frac{\partial v_x}{\partial n} = -\left[\frac{\partial\gamma}{\partial x}+\kappa\frac{\partial}{\partial x}\left(\frac{\partial v_t}{\partial t}+\frac{\partial v_x}{\partial x}\right)+\varepsilon\left(\frac{\partial^2 v_x}{\partial t^2}+\frac{\partial^2 v_x}{\partial x^2}\right)\right], \tag{8}$$

where $\frac{\partial\gamma}{\partial x}$ includes both the driving thermocapillary stress and the solutocapillary stress, ε is the surface shear viscosity, κ is the surface dilational viscosity, and (v_n,v_t,v_x) are the velocity components in the local basis.

Using the notation $\frac{\partial\gamma}{\partial x} = \frac{\partial\gamma}{\partial T}\frac{\partial T}{\partial x} - \left|\frac{\partial\gamma}{\partial\Gamma}\right|\frac{\partial\Gamma}{\partial x} = (\partial_x\gamma)_\Gamma - |\partial_x\gamma|_T = (\partial_x\gamma)_\Gamma(1-r_\mathrm{e})$ with subscripts Γ and T indicating the constant surface concentration and temperature, respectively, and where the ratio $r_\mathrm{e} = |\partial_x\gamma|_T/(\partial_x\gamma)_\Gamma$ (with subscript e for elasticity) compares the damping Gibbs Marangoni stress to the driving thermocapillary stress, eqn (8) can be written as a function of a single theoretical damping factor r^th:

$$\eta\frac{\partial v_x}{\partial n} = -(\partial_x\gamma)_\Gamma\left[1 - r_\mathrm{e} + \frac{\kappa+\varepsilon}{(\partial_x\gamma)_\Gamma}\frac{\partial^2 v_x}{\partial x^2} + \frac{\varepsilon}{(\partial_x\gamma)_\Gamma}\frac{\partial^2 v_x}{\partial t^2}\right], \tag{9}$$

$$= -(\partial_x\gamma)_\Gamma(1 - r^\mathrm{th}) \tag{10}$$

Here we neglect the tangential velocity v_t in comparison with v_x. This equation, together with the Stokes equation in the bulk, governs the fluid motion and thus the drainage dynamics. All the rheological properties of the interface are included in the correction $(1 - r^\mathrm{th})$ to the driving force $(\partial_x\gamma)_\Gamma$. Since we are in the linear regime (inset of Fig. 3), a multiplicative correction to the force induces the same multiplicative correction to the system response. The parameter r^th hence provides a theoretical prediction for the experimental parameter r defined in eqn (4).

As r remains smaller than 0.17, we consider it to be a small correction to the unperturbed drainage. The velocity then scales as $U \sim \alpha_0\frac{e}{\eta}\left(\frac{\partial\gamma}{\partial x}\right)_\Gamma$ (see eqn (3)). From this we deduce:

$$\frac{\varepsilon}{(\partial_x\gamma)_\Gamma}\frac{\partial^2 v_x}{\partial t^2} \sim \frac{\varepsilon}{e^2}\frac{\varepsilon}{(\partial_x\gamma)_\Gamma} \sim \alpha_0 B_\mathrm{q}^\mathrm{s} \text{ with } B_\mathrm{q}^\mathrm{s} = \frac{\varepsilon}{\eta e} \tag{11}$$

$$\frac{(\kappa+\varepsilon)}{(\partial_x\gamma)_\Gamma}\frac{\partial^2 v_x}{\partial x^2} \sim \frac{(\kappa+\varepsilon)}{R^2}\frac{U}{(\partial_x\gamma)_\Gamma} \sim \alpha_0 B_\mathrm{q}^\mathrm{d} \text{ with } B_\mathrm{q}^\mathrm{d} = \frac{e(\kappa+\varepsilon)}{\eta R^2} \tag{12}$$

It is clear from this analysis that the global damping factor r^th is a function of three non-dimensional numbers:

$$r^\mathrm{th} = f(r_\mathrm{e}, B_\mathrm{q}^\mathrm{s}, B_\mathrm{q}^\mathrm{d})$$

where r_e is a retardation factor due to the Gibbs elasticity, B_q^s is the Boussinesq number based on the surface shear viscosity and B_q^d is the Boussinesq number associated with the extension of the film. We will now examine each of those contributions separately.

4.1 Contribution of the Gibbs elasticity

We first disregard the influence of surface viscosity, to focus on the solutocapillary contribution in eqn (10). A sketch of the surfactant transport mechanism is presented in Fig. 6. We consider the surfactant transport along a meniscus oriented along x. The adsorbed surfactants of concentration Γ are advected by the interface velocity $U_s \sim \alpha_0 e(\partial_T\gamma\partial_x T)/\eta$, inducing a flux $\Phi^1_{\text{conv}} \sim (\Gamma U_s)e$ for each meniscus. Similarly, the surfactants in the bulk, of concentration c, generate a flux $\Phi^{\text{bulk}}_{\text{conv}} \sim (cU)e^2$. At the front end of a bubble, the x-component of the bulk velocity is not strongly modified, but that of the interface velocity tends to zero for geometrical reasons. The convective flux Φ^1_{conv} thus vanishes too. Experimentally, the exponential decay of the liquid fraction (before the sudden saturation at t_s) is the indication of a constant value of the parameter r. This means that the solutocapillary effect is constant during the whole drainage process, *i.e.* the concentration at the interface is steady, and the surfactant flux along x is independent of x. A classical assumption is that a counterflow in the thin films balances Φ^1_{conv}.[17] However, in our specific geometry, there is no thin film between the bubbles, and the mobility of the wetting films is very small due to the no slip condition at the cell wall. The vanishing flux Φ^1_{conv} at the end of the meniscus must therefore be compensated by a flux in the same direction and of the same amplitude across the liquid phase located at the end of the meniscus (see Fig. 6). In other words, the surfactants flow along the bubble interface and, upon reaching the front of the bubble, they have to diffuse through the solution to reach the next bubble downstream:

$$\Phi^1_{\text{conv}} = \Phi^{1\to2}_{\text{diff}} \tag{13}$$

where $\Phi^{1\to2}_{\text{diff}}$ is the diffusive flux of DOH across the liquid phase between two adjacent bubbles, labelled bubble 1 and bubble 2. The diffusion field is coupled to the complex geometry of the meniscus and the vertex network, and to the convection by the bulk velocity. We examined three modes of surfactant transport between bubbles: diffusion across the meniscus, diffusion across the films, and convection across the meniscus. However, the scaling laws from the latter two models are not in agreement with our experimental data, and this part of the analysis has been moved to the ESI.† We focus here on the first of these three models.

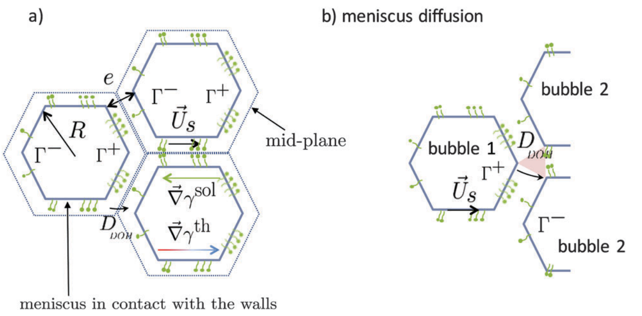

Fig. 6 (a) Sketch representing the solutocapillary stress induced by the DOH molecules. pPb refers to the pseudo-Plateau borders.[20] (b) Diffusion of the surfactant across the meniscus.

We consider the diffusion across a meniscus of characteristic size e^3. The surfactants diffuse through a section e^2 and the concentration gradient scales as $\Delta c/e$, where Δc is the difference in DOH bulk concentration between the front of bubble 1 and the rear of bubble 2. We get $\Phi^{1\to2}_{\text{diff}} \sim (D_{\text{DOH}}\Delta c/e)e^2$, where D_{DOH} is the diffusion coefficient of DOH in water. The parameter Δc involved in this expression is also the concentration difference between the two ends of a given meniscus, and obeys $\Delta c \sim R(\partial_x\gamma)_T/(\partial_c\gamma)$, assuming a fast equilibration of the interface with the subphase. From this, we deduce the expression of $(\partial_x\gamma)_T$ and the relation:

$$r^{\text{th}}_{\text{D},1} \sim \frac{\alpha_0\Gamma(c)\left|\dfrac{\partial\gamma_{\text{eq}}}{\partial c}\right|}{\eta D_{\text{DOH}}} \times \frac{e}{R}. \tag{14}$$

The scaling law in e/R is in very good agreement with the experimental results shown in Fig. 7, in which e and R varied independently.

Based on the literature, we take $D_{\text{DOH}} = 5 \pm 2 \times 10^{-9}$ m^2 s^{-1} for the diffusion coefficient of DOH in water.[26] Our measurements of $\partial_c\gamma_{\text{eq}}$ show that the equilibrium surface tension evolves linearly with the DOH bulk concentration: $\partial\gamma_{\text{eq}}/\partial c = 1$ N m^2 mol^{-1} (see Fig. 2 in the ESI†). Lastly, the concentration at the interface is given by a Langmuir isotherm:[27,28]

$$\Gamma(c) = \Gamma_\infty\frac{Kc}{1+Kc} \tag{15}$$

with $\Gamma_\infty = 5.53 \times 10^{-6}$ mol m^2 and $K = 2.86 \times 10^5$ L mol^{-1} (see ESI,† and ref. 29). Now that all the terms are known, and eqn (14) can be directly compared to the experimental results with a dimensionless prefactor A as the only adjustable parameter. As shown in Fig. 7, the best fit is obtained for $A \sim 1.5 \times 10^{-4}$.

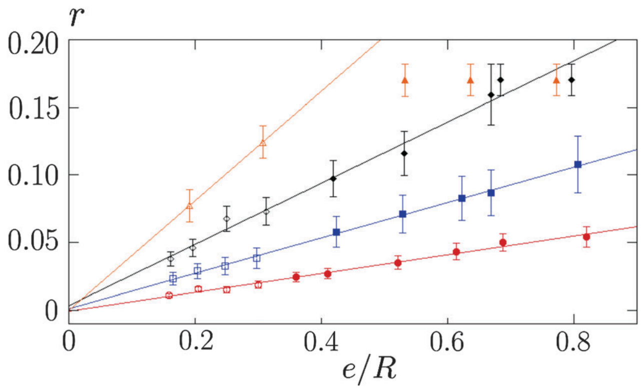

Fig. 7 Evolution of r as a function of the ratio e/R for different DOH concentrations: 1.6×10^{-6} mol L^{-1} (circles), 3.2×10^{-6} mol L^{-1} (squares), 5.6×10^{-6} mol L^{-1} (diamonds) and 9.6×10^{-6} mol L^{-1} (triangles). For each dataset, the hollow (resp. solid) symbols correspond to e = 19.3 μm (resp. e = 54.2 μm). Solid lines represent the fitting curves based on eqn (14) in the linear regime for $A = 1.5 \times 10^{-4}$, without any other fit parameter.

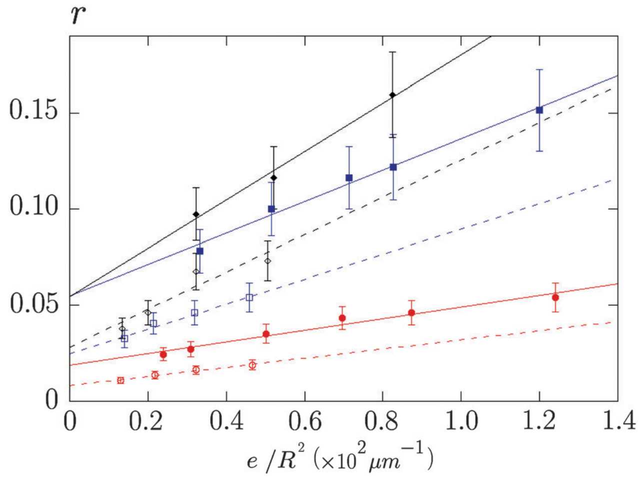

Fig. 8 Evolution of r as a function of e/R^2 for different DOH concentrations: 1.6×10^{-6} mol L^{-1} (circles), 3.2×10^{-6} mol L^{-1} (squares) and 5.6×10^{-6} mol L^{-1} (diamonds). For each dataset, the hollow (resp. solid) symbols correspond to e = 19.3 μm (resp. e = 54.2 μm). Dashed (resp. solid) lines represent the best linear fitting curves for e = 19.3 μm (resp. e = 54.2 μm), for each dataset.

The functional dependency of r with the 3 independent parameters e, R and $\partial T/\partial x$ is accurately captured by this model in the linear regime. However, A is surprisingly small: the model fails to even remotely predict the order of magnitude of the delay in drainage. A possible explanation for it is that Γ does not reach its equilibrium value $\Gamma(c)$. The interface elements are created at the rear of the bubble (interface extension zone) and disappear at the front (interface compression zone). The lifetime of these interface elements is thus of the order of $U/R \sim 1$ s, which is much shorter than the equilibration time of the interface, of about 20 s (see ESI†). A smaller average value of Γ, independent of the geometry, might explain our data.

4.2 Contribution of the surface viscosities

We now consider the damping to be dominated by viscous effects rather than by an elastic effect. The first contribution of the surface viscosity to the damping factor r scales as (eqn (10) and (11)):

$$r_{\rm dil}^{\rm th} \sim \frac{(\kappa+\varepsilon)}{\eta}\frac{e}{R^2}. \tag{16}$$

The experimental values of r from Fig. 4 are shown in Fig. 8 as a function of e/R^2. For a given cell height e, the general trend is consistent with such a scaling, however the data do not collapse on a single curve at a fixed DOH concentration when e and R vary. Furthermore, the curves are not linear. The intercept corresponds to an offset that could be imputed to the surface shear viscosity. Indeed, eqn (10) and (11) give the following scaling for its contribution to the damping factor:

$$r_{\rm sh}^{\rm th} \sim \frac{\varepsilon}{\eta e} \tag{17}$$

However, the offset increases with e for a given DOH concentration, in contradiction with the prediction from eqn (17). Finally, even though this model cannot recover a scaling law consistent with our experiments, it does predict a much better order of magnitude for the delay r: with $\varepsilon \sim 10^{-7}$ kg s^{-1} we get $\varepsilon e/(\eta R^2) \sim 0.1$.

4.3 Synthesis

Table 1 shows the scalings for the contributions examined here and in the ESI,† with the exception of Gibbs elasticity with convection across the meniscus since it turns out to be negligible (see ESI†). We find that the best fit is $r \sim e/R$, *i.e.* Plateau border cross-section/length, which may correspond to a dominating elastic contribution. However a prefactor of order 10^{-4} indicates that the surfactant transport process is faster than simple diffusion in the meniscus between adjacent bubbles. A more consistent order of magnitude is given by the model for Gibbs elasticity with diffusion of surfactants across the films, or by the viscous model; however neither of those predicts a scaling for r with e and R in agreement with the experimental data.

5 Conclusion

In this work, we investigated the effect of surface rheology on a thermally driven foam in a microfluidic cell. Such an experimental setup allows for a simple foam geometry (monodisperse and 2D), the parameters of which can be tuned with great accuracy. We investigated the level of contribution of different surface rheological properties arising from the presence of a poorly soluble surfactant at the interface: (i) the surface shear viscosity, which was expected to be enhanced in a microfluidic experiment where the velocity is zero at the walls and maximal in the mid-plane of the Hele-Shaw cell, (ii) the surface dilational viscosity expected in any drainage experiment, since convecting interfaces requires their creation at the rear of the bubbles and their destruction at the front, and (iii) the Gibbs Marangoni stress induced by the thermocapillary surface flow. We characterised the drainage dynamics by defining a damping parameter

Table 1 Different scaling laws for the contributions to the damping factor r

	Gibbs elasticity		Surface viscosity	
	Diff. – meniscus	Diff. – film	$B_{\rm q}^{\rm s}$	$B_{\rm q}^{\rm d}$
Scaling law for r	$\frac{\alpha_0\Gamma_\infty\left\lvert\frac{\partial\gamma_{\rm eq}}{\partial c}\right\rvert}{\eta D_{\rm DOH}}\times\frac{Kc}{1+Kc}\times\frac{e}{R}$	$\frac{\alpha_0\Gamma_\infty\sqrt{h}\left\lvert\frac{\partial\gamma_{\rm eq}}{\partial c}\right\rvert}{\eta D_{\rm DOH}}\times\frac{Kc}{1+Kc}\times\frac{e^{3/2}}{R^2}$	$\frac{2\varepsilon}{\eta e}$	$\frac{(\kappa+\varepsilon)}{2\eta}\frac{e}{R^2}$
Observations				
+	Consistent scaling,	Consistent trend		Consistent trend
−	prefactor too small	requires the intercept (offset increasing with e)	Scaling independent of R wrong trend for the intercept ($R \to \infty$)	requires the intercept (offset increasing with e)

r encompassing these three contributions. We derive scaling laws for r in terms of the geometrical parameters e and R for each of the damping mechanisms, and find the best agreement with the pure elastic damping model. However, the order of magnitude of r predicted by this model differs strongly from the experimental values, whereas considering only viscous effects gives a prediction closer to the experimental data, but the wrong scaling. We conclude that the damping at work is likely to be a more complex mechanism, involving an interplay between several of these contributions. Our study paves the way towards a deeper investigation in that direction.

Acknowledgements

We acknowledge valuable discussions and experiments with Delphine Hannoy. The thermocapillary drainage has been patented under the reference PCT/EP2014/079337. This work has been supported by CNRS, Direction Générale de l'Armement (DGA), IPGG Equipex ANR-10-EQPX-34, ESPCI ParisTech, Dim-NanoK région Ile de France, and ANR under the grant 13-BS09-0011-01.

References

1 R. Farajzadeh, A. Andrianov and P. L. J. Zitha, *Ind. Eng. Chem. Res.*, 2010, **49**, 1910–1919.
2 R. Liontas, K. Ma, G. J. Hirasaki and S. L. Biswal, *Soft Matter*, 2013, **9**, 10971.
3 C.-C. Wang, K.-C. Yang, K.-H. Lin, H.-C. Liu and F.-H. Lin, *Biomaterials*, 2011, **32**, 7118–7126.
4 C. Colosi, M. Costantini, A. Barbetta, R. Pecci, R. Bedini and M. Dentini, *Langmuir*, 2013, **29**, 82–91.
5 E. Chevallier, A. Saint-Jalmes, I. Cantat, F. Lequeux and C. Monteux, *Soft Matter*, 2013, **9**, 7054–7060.
6 S. A. Koehler, S. Hilgenfeldt and H. A. Stone, *Langmuir*, 2000, **16**, 6327–6341.
7 S. A. Koehler, S. Hilgenfeldt and H. Stone, *J. Colloid Interface Sci.*, 2004, **276**, 420–438.
8 D. Langevin, *ChemPhysChem*, 2008, **9**, 510–522.
9 L. Leonard, *AIChE J.*, 1965, **11**, 18–25.
10 D. Weaire, N. Pittet, S. Hutzler and D. Pardal, *Phys. Rev. Lett.*, 1993, **71**, 2670.
11 S. A. Koehler, S. Hilgenfeldt and H. A. Stone, *Phys. Rev. Lett.*, 1999, **82**, 4232.
12 I. Cantat, S. Cohen-Addad, F. Elias, F. Graner, R. Höhler, O. Pitois, F. Rouyer and A. Saint-Jalmes, *Foams: structure and dynamics*, Oxford University Press, 2013.
13 V. Carrier, S. Destouesse and A. Colin, *Phys. Rev. E: Stat., Nonlinear, Soft Matter Phys.*, 2002, **65**, 061404.
14 A. Saint-Jalmes, *Soft Matter*, 2006, **2**, 836–849.
15 D. A. Edwards, H. Brenner and D. T. Wasan, *Interfacial Transport Processes and Rheology*, Butterworth-Heinemann, Chemical Engineering edn, 1991.
16 M. Durand and D. Langevin, *Eur. Phys. J. E: Soft Matter Biol. Phys.*, 2002, **7**, 35–44.
17 E. Lorenceau, N. Louvet, F. Rouyer and O. Pitois, *Eur. Phys. J. E: Soft Matter Biol. Phys.*, 2009, **28**, 293–304.
18 J. Marchalot, J. Lambert, I. Cantat, P. Tabeling and M.-C. Jullien, *Europhys. Lett.*, 2008, **83**, 64006.
19 C. Gay, P. Rognon, D. Reinelt and F. Molino, *Eur. Phys. J. E: Soft Matter Biol. Phys.*, 2011, **34**, 1–11.
20 V. Miralles, B. Selva, I. Cantat and M.-C. Jullien, *Phys. Rev. Lett.*, 2014, **112**, 238302.
21 Y. Xia and G. M. Whitesides, *Annu. Rev. Mater. Sci.*, 1998, **28**, 153–184.
22 B. Selva, J. Marchalot and M.-C. Jullien, *J. Micromech. Microeng.*, 2009, **19**, 065002.
23 N.-S. Cheng, *Ind. Eng. Chem. Res.*, 2008, **47**, 3285–3288.
24 A. Saint-Jalmes, Y. Zhang and D. Langevin, *Eur. Phys. J. E: Soft Matter Biol. Phys.*, 2004, **15**, 53–60.
25 L. Scriven, *Chem. Eng. Sci.*, 1960, **12**, 98–108.
26 D. S. Valkovska and K. D. Danov, *J. Colloid Interface Sci.*, 2000, **223**, 314–316.
27 E. Lucassen-Reynders, A. Cagna and J. Lucassen, *Colloids Surf., A*, 2001, **186**, 63–72.
28 I. Langmuir, *J. Am. Chem. Soc.*, 1918, **40**, 1361–1403.
29 J. Lu, I. Purcell, E. Lee, E. Simister, R. Thomas, A. Rennie and J. Penfold, *J. Colloid Interface Sci.*, 1995, **174**, 441–455.